# On-board Bluetooth-based Relative Localization for Collision Avoidance in Micro Air Vehicle Swarms

M. Coppola[1,†], K.N. McGuire[†], K.Y.W. Scheper[†], and G.C.H.E. de Croon[2,†].

arXiv:1609.08811v1 [cs.RO] 28 Sep 2016

***Abstract*— A current limitation of using Micro Air Vehicles (MAVs) in teams is the high risk of collisions between members. Knowledge of relative location is needed in order to facilitate evasive maneuvers. We propose an on-board Bluetooth-based relative localization method. Bluetooth is a light-weight and energy efficient communication technology that is readily available on even the smallest MAV units. In this work, it is exploited for communication between team members to exchange on-board states (velocity, height, and orientation), while the strength of the communication signal is used to infer relative range. The data is fused on-board by each drone to obtain a relative estimate of the location and motion of all other team members. Furthermore, a collision avoidance controller is proposed based on collision cones. It is designed to deal with the expected relative localization errors by adapting the collision cones during flight and enforcing a clock-wise evasion maneuver. The system was tested with a team of AR-Drones 2.0 flying in a 4m×4m arena at the same height. The system showed promising results. When using two AR-Drones and off-board velocity/orientation estimates, the drones were able to fly around the arena for a cumulative time of 25 minutes with only one collision. With three AR-Drones under the same conditions, flight time to collision was 3 minutes. With two AR-Drones flying with on-board velocity estimation, the time to collision was approximately 3 minutes due to the disturbances in velocity estimates. Simulations show that even better results can be expected with smaller MAVs.**

## I. INTRODUCTION

Micro Air Vehicle (MAV) applications include surveillance [1], mapping [2], and inspection of buildings [3][4] or other infrastructure [5]. State-of-the-art technology has led to miniaturized MAVs such as the Lisa-S Ladybird [6] or the Pico-Quadrotor [7]. These platforms benefit from: lower mass, increased portability, less obtrusive/restricted navigation in indoor environments, and safer use near humans. However, these smaller platforms also suffer from highly limited sensing and computational capabilities. Allowing several MAVs to operate in a team/swarm improves their performance by reducing the task execution time and adding robustness, scalability, and flexibility [8] [9].

Swarm behavior can emerge with fully independent units that have no awareness of each-other [10]. However, when a team of MAVs with decentralized control performs an arbitrary task in a confined indoor space, there is a non-negligible risk of intra-swarm collisions [11]. This is a failure condition to be avoided to ensure mission success. Collision avoidance is facilitated by on-board knowledge by each MAV of the relative location of close-by team members. Additionally, knowledge of relative location can empower more complex team behaviors such as leader-follower [7] or formation-flying [12].

One method for relative localization is to rely on a shared reference frame in which each MAV can localize itself. The MAVs can then communicate, compare their position coordinates, and infer a relative estimate. In outdoor tasks, Global Positioning System (GPS) receivers can be used to obtain global position data that is then shared [13][14], but this does not function indoors [15]. In order to achieve the same effect without compromising the aforementioned efforts of MAV miniaturization, several solutions propose planting external sensors/beacons with known relative locations, such as: motion tracking cameras [16], fixed wireless transmitters/receivers [17], or fixed visual markers [18]. Although effective, these solutions defeat the purpose of an exploratory task by relying on a pre-arranged environment. The Simultaneous Localization and Mapping (SLAM) strategy and its variants attempt to solve this by generating a common map on-board during flight [2]. However, when map generation is not part of the mission, then this is a resource intensive practice to be discouraged [19], or even beyond the current capabilities of miniaturized MAVs [6].

The use of direct measurements between MAVs overcomes these disadvantages. Vision has received attention, but examples found in literature simplify the detection task by adopting mounted visual aids in the form of: colored balls [20], tags [21], or markers [22]. These studies benefit from the combination of relatively high-resolution cameras, fast processing speeds, and large markers if compared to more miniaturized drones. However, test results in the exploratory phases of this study have led to the conclusion that using vision without such aids and at lower resolutions (128×96px, as seen on the Lisa-S Ladybird [23] [24]) becomes highly problematic and prone to false-positives/false-negatives. Furthermore, performance is dependent on lighting conditions, which may change. Other disadvantages of using vision are: the need for a front-facing camera and flight along its axis, limited field-of-view, and generally high processing requirements. Infra-Red (IR) sensors have been proposed as an alternative but these require multiple units to be arranged in a rigid

[1]m.coppola@tudelft.nl
[2]g.c.h.e.decroon@tudelft.nl
[†] Micro Air Vehicle Laboratory, Faculty of Aerospace Engineering, Delft University of Technology, Kluyverweg 1, 2629 HS Delft, The Netherlands

structure, leading to a high mass and power consumption penalty [25].

The work in [26] attempts to overcome the issues above by using on-board sound-based localization with a mounted microphone array. The difference between arrival times at the different receivers is used to infer the relative bearing. A passive version of this attempted to locate propeller sounds of nearby MAVs, yet this suffered from noise coming from the MAV's own engine. The issue was overcome by the introduction of a chirp generator to send audio signals at specific frequencies [27]. Nevertheless, the method still suffers from noise induced by turbulence, as well as structural vibrations which compromise the rigidity of the microphone array [28]. Furthermore, a dedicated microphone array and chirp generator must be mounted. For smaller MAVs, this can account for an increase in mass of 10%-20% [28] [6].

Alternatively, a component that is almost always already present on all MAVs is a wireless transceiver. This is generally used for communication with a ground station [29] [23], but it may also be used for intra-swarm communication [11]. The signal strength of a wireless communication decreases with distance from the antenna, and can be used as a measure for range between MAVs. This knowledge has already been exploited on-board of MAVs by attempting collision avoidance using only relative range sensing [11]. However, range-only relative estimates, coupled with the significant noise and disturbances, were insufficient to guarantee safe flight of two or more MAVs in a confined area.

**The contribution in this article is an *on-board relative localization* method for MAVs based on intra-swarm wireless communication**. This was implemented using Bluetooth antennas, which are readily available at a low mass, power, and cost penalty even on smaller MAVs [23]. In this work, Bluetooth intra-swarm communication is used as a method for the exchange of own state measurements *and* as a measure of relative range (based on the received signal strength). This allows each MAV to estimate the relative location of the others. The advantages of this solution are:a) it provides a relative location estimate at all relative bearings; b) it has a low dependence on the lighting and sound conditions of the environment; c) it has low energy consumption requirements; d) it does not require the addition of any dedicated sensors. **A reactive collision avoidance strategy tailored to the localization estimates is also proposed.** It is based on the concept of collision cones [30] [31] but designed to deal with the expected localization errors.

The remainder of this article is organized as follows. Section II introduces the relative localization method. Section III describes the collision avoidance strategy implemented in the MAVs. Tests have been performed in simulation and in the real-world using Bluetooth equipped AR-Drones 2.0 to determine the performance of the system with respect to collision avoidance. The test environments and methodologies used are defined in Section IV. All results are described in Section V and further discussed in Section VI. Section VII provides concluding remarks.

## II. BLUETOOTH-BASED RELATIVE LOCALIZATION

In this work, collision avoidance is achieved using lateral evasive maneuvers only. Lateral avoidance is preferred over height separation in order to limit aerodynamic disturbances between MAVs [32] [16]. For this reason, there is a need to determine a full location estimate, the method for which is explained in this section.

Localization is enabled via direct communication between the MAVs, which communicate the following on-board states to each-other: planar velocity in the body frame, orientation with respect to North, and height from the ground. With Bluetooth communication, an MAV also measures the Received Signal Strength Indication (RSSI), indicating the range between the antennas. Each MAV fuses the received states, the RSSI, and its own on-board states to estimate the full relative position of the other MAV. When multiple MAVs are present, multiple instances of the fusion filter run in parallel so that each MAV may keep track of the others.

Section II-A introduces the general localization framework and relevant variables. Section II-B discusses the relationship between RSSI and range. Section II-C explains how the fusion filter is set-up, and Section II-D presents the results of a preliminary test.

### A. Framework Definition for Relative Localization

Consider two MAVs $\mathcal{R}_i$ and $\mathcal{R}_j$ with right-handed body-fixed frames $\mathcal{F}_{B_i}$ and $\mathcal{F}_{B_j}$, respectively. See Figure 1 for an illustration.

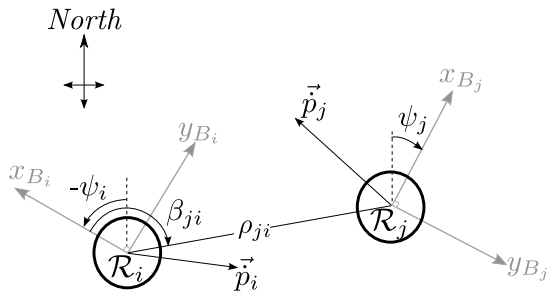


Fig. 1: Top view of the relative localization framework of MAV $\mathcal{R}_j$ by MAV $\mathcal{R}_i$. $x_B$ and $y_B$ are the axis of the body frame $\mathcal{F}_B$. $z_B$ is positive down-wards (into the page). $\psi$ denotes the orientation with respect to North. $\rho_{ji}$ is range between the origins of $\mathcal{F}_{B_i}$ and $\mathcal{F}_{B_j}$. $\beta_{ji}$ is the horizontal planar bearing of the origin of $\mathcal{F}_{B_j}$ with respect to $\mathcal{F}_{B_i}$.

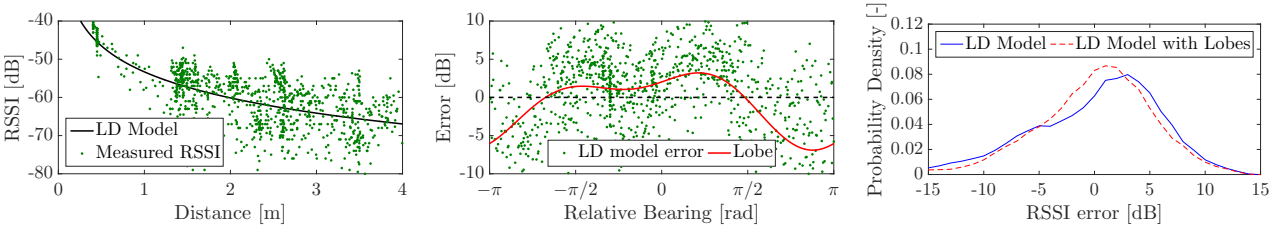


(a) RSSI measurements with respect to distance (green-dotted) and fitted Log-Distance model (black, solid).

(b) Error of LD model with respect to relative bearing (green, dotted) fitted with a second order Fourier series (red, solid).

(c) Noise about the LD model without (blue, solid) and with (red, dashed) lobe impact.

Fig. 2: Results of RSSI measurements during an experiment whereby a Bluetooth-enabled Ladybird MAV was carried in circles around a fixed Bluetooth antenna. The heading of the Ladybird MAV was kept constant so as to explore the impact of relative bearing on the model error.

The relative location of $\mathcal{R}_j$ with respect to $\mathcal{R}_i$ can be defined as:

$$\vec{\mathcal{P}}_{ji} = \begin{bmatrix} x_{ji} & y_{ji} & z_{ji} & \phi_{ji} & \theta_{ji} & \psi_{ji} \end{bmatrix}. \tag{1}$$

$\vec{\mathcal{P}}_{ji}$ is a vector of the quantities describing the 3-Dimensional (3D) relative pose of $\mathcal{R}_j$ with respect to $\mathcal{R}_i$. It is expressed in $\mathcal{F}_{B_i}$. $x_{ji}$, $y_{ji}$, and $z_{ji}$ are the position of the origin of $\mathcal{R}_j$ in $\mathcal{F}_{B_i}$; $\phi_{ji}$, $\theta_{ji}$, and $\psi_{ji}$ are the roll, pitch, and yaw angles of $\mathcal{F}_{B_j}$ with respect to $\mathcal{F}_{B_i}$.

Pitch and roll may be neglected by assuming that quadrotors maintain approximately planar orientations with respect to the ground. $\vec{\mathcal{P}}_{ji}$ may then be re-defined as:

$$\vec{\mathcal{P}}_{ji} = \begin{bmatrix} \rho_{ji} & \beta_{ji} & h_{ji} & \psi_{ji} \end{bmatrix}. \tag{2}$$

Where: $\rho_{ji}$ represents the range between the origins of $\mathcal{F}_{B_i}$ and $\mathcal{F}_{B_j}$, see Equation 3; $\beta_{ji}$ is the horizontal planar bearing of the origin of $\mathcal{F}_{B_j}$ with respect to $\mathcal{F}_{B_i}$, see Equation 4; $h_{ji}$ is the height of $\mathcal{R}_j$ with respect to $\mathcal{R}_i$; $\psi_{ji}$ is the orientation of $\mathcal{R}_j$ with respect to $\mathcal{R}_i$.

$$\rho_{ji} = \sqrt{x_{ji}^2 + y_{ji}^2 + h_{ji}^2} \tag{3}$$

$$\beta_{ji} = atan2(y_{ji}, x_{ji}) \tag{4}$$

### B. Signal Strength as a Range Measurement

Let $m_{\rho_{ji}}$ be the RSSI measurement (in $dB$) correlated with $\rho_{ji}$ by a function $\mathcal{L}(\rho_{ji})$. The signal strength may be modeled according to the Log-Distance (LD) model [33]:

$$m_{\rho_{ji}} = \mathcal{L}(\rho_{ji}) = P_n - 10 \cdot \gamma_l \cdot \log_{10}(\rho_{ji}). \tag{5}$$

In Equation 5: $P_n$ is the signal strength in dB at a nominal distance of 1 meter, and $\gamma_l$ is the *space-loss parameter*. It dictates the decay of the signal's power with distance. For free-space: $\gamma_l = 2.0$. Experimentally, it has been found that office buildings can feature $2 \leq \gamma_l \leq 6$ [34]. A sensitivity analysis of the model showed that an accurate identification of $\gamma_l$ has a low impact on the distance estimate at lower distances (which is the scope of this article). The LD model is generally assumed subject to a Zero-Mean Gaussian Noise (ZMGN) [35] [36].

We analyzed the LD model with a Bluetooth-enabled Ladybird MAV [6] and a fixed omni-directional Bluetooth antenna (W1049B by Pulse [37]). The Ladybird MAV was carried in concentric circles at different distances around the antenna. Its orientation was kept constant so as to vary relative bearing throughout the measurements. The results from a representative data-sample are presented in Figure 2, to which the LD model is fitted using a non-linear Least Squares (LS) estimator as in Figure 2a. Among a set of similar experiments, the standard deviation of the error about the fitted LD model was found to be between $3dB$ and $6dB$. This is in line with the findings from [11] and [38].

Figure 2b shows the error of the LD model as a function of the relative bearing. The presence of antenna lobes is discerned [11]. This knowledge suggests an extension of the LD model with an additional gain term that is a function of relative bearing [11], but this is rejected. Including a term that is dependent on bearing means that a change in RSSI can be ambiguously associated to a change in either bearing or range. Furthermore, the shape of the lobes was found to be antenna-specific when tested with different MAVs. Figure 2c shows the error distribution, where a clear skew is present. A model that includes the lobe from Figure 2b is seen to reduce the skew. Other disturbances may be caused by: the interference by the reflection of the signal in the environment [33] [36], the presence of other signals in the $2.4GHz$ spectrum [34] [39], or other objects that obstruct the signal [34].

### C. Localization via Fusion of Range and On-board States

Achieving a relative localization estimate requires measuring or inferring the quantities in $\vec{\mathcal{P}}_{ji}$. Thanks to inter-drone communication, $h_{ji}$ and $\psi_{ji}$ are trivially observable by an MAV $\mathcal{R}_i$ by taking the difference between its own on-board state and the received states from $\mathcal{R}_j$:

$$h_{ji} = h_j - h_i, \tag{6}$$

$$\psi_{ji} = \psi_j - \psi_i. \tag{7}$$

$\psi_i$ and $\psi_j$ are the rotations of $\mathcal{F}_{B_i}$ and $\mathcal{F}_{B_j}$ with respect to a common reference axis. The common axis, as depicted in Figure 1, is magnetic North. It is measurable by all

MAVs using a magnetometer [40] [41]. $h_j$ and $h_i$ are the height of the origin of $\mathcal{F}_{B_i}$ and $\mathcal{F}_{B_j}$ with respect to a reference height. It could be measured using a pressure sensor [42] [43] [44] and/or a downward-facing camera [45] [46]. Finally, $\rho_{ji}$ is available thanks to RSSI measurements, which are correlated with range as elaborated in Section II-B.

When $h_{ji}$, $\psi_{ji}$, and $\rho_{ji}$ are measured, the relative bearing $\beta_{ji}$ becomes observable [47] [48]. We use a discrete-time Extended Kalman Filter (EKF) in order to perform sensor fusion and observe $\beta_{ji}$. The EKF is chosen due to its efficient processing and memory requirements [49]. Let Equation 8 be the state transition model from time step $k$ to $k+1$.

$$\begin{bmatrix} \vec{p}_{ji} \\ \dot{\vec{p}}_i \\ \dot{\vec{p}}_{jRi} \\ \psi_j \\ \psi_i \\ h_j \\ h_i \end{bmatrix}_{k+1} = \begin{bmatrix} \vec{p}_{ji} + \left(\dot{\vec{p}}_{jRi} - \dot{\vec{p}}_i\right)\Delta t \\ \dot{\vec{p}}_i \\ \dot{\vec{p}}_{jRi} \\ \psi_j \\ \psi_i \\ h_j \\ h_i \end{bmatrix}_k + \vec{v}_k \tag{8}$$

$\vec{p}_{ji} = \begin{bmatrix} x_{ji} & y_{ji} \end{bmatrix}^T$ holds Cartesian estimates of bearing and range. $\dot{\vec{p}}_i = \begin{bmatrix} \dot{x}_i & \dot{y}_i \end{bmatrix}^T$ is a vector of the velocity of $\mathcal{R}_i$ in $\mathcal{F}_{B_i}$ (see Figure 1). $\dot{\vec{p}}_{jRi}$ is $\dot{\vec{p}}_j$ *rotated* from $\mathcal{F}_{B_j}$ to $\mathcal{F}_{B_i}$. $\Delta t$ is a discrete time step between updates equal to the time between $k$ and $k+1$. $\vec{v}_k$ represents the noise in the process at time step $k$. This state transition model assumes that all current velocities and orientations remain constant. The observation model for the EKF is given by Equation 9.

$$\begin{bmatrix} m_{\rho_{ji}} \\ \vec{p}_i \\ \dot{\vec{p}}_j \\ \psi_j \\ \psi_i \\ h_j \\ h_i \end{bmatrix}_k = \begin{bmatrix} \mathcal{L}(\rho_{ji}) \\ \vec{p}_i \\ \mathbf{R_{2D}}(\psi_{\mathbf{ji}}) \cdot \dot{\vec{p}}_{jRi} \\ \psi_j \\ \psi_i \\ h_j \\ h_i \end{bmatrix}_k + \vec{w}_k \tag{9}$$

$m_{\rho_{ji}}$ is a measurable quantity that is correlated with $\rho_{ji}$. In this case $m_{\rho_{ji}}$ is the measured RSSI in $dB$ during communication, which is a function of the range $\rho_{ji}$ as given by $\mathcal{L}(\rho_{ji})$, see Equation 5. $\mathbf{R_{2D}}(\cdot)$ is a 2D rotation matrix that uses the relative heading $\psi_{ji}$ to rotate the state estimate $\dot{\vec{p}}_{jRi}$ from $\mathcal{F}_{B_i}$ to $\mathcal{F}_{B_j}$. $\vec{w}_k$ represents the noise in the measurements at time step $k$. Note that $\rho_{ji}$ is expanded as per Equation 3 so as to observe $x_{ji}$ and $y_{ji}$.

In the EKF, the measurement noise matrix $\mathbf{R}$ is a diagonal matrix with the form shown in Equation 10.

$$\mathbf{R} = \begin{bmatrix} \sigma_m^2 & & & \\ & \sigma_v^2 \cdot \mathbf{I_{4\times 4}} & & \\ & & \sigma_\psi^2 \cdot \mathbf{I_{2\times 2}} & \\ & & & \sigma_h^2 \cdot \mathbf{I_{2\times 2}} \end{bmatrix}. \tag{10}$$

$\sigma_m$ is the expected standard deviation of the noise on $m_{\rho_{ji}}$. $\sigma_v$ is the expected standard deviation of the noise on $\dot{\vec{p}}_i$ and $\dot{\vec{p}}_j$. $\sigma_\psi$ is the expected standard deviation of the magnetic orientation measurements. $\sigma_h$ is the expected standard deviation of the height measurements. $\mathbf{I_{n\times n}}$ is an $n \times n$ identity matrix such that the same standard deviation transfers to the relevant variables.

Considering the noise analysis of the LD model discussed in Section II-B, a foreseen disadvantage of using the EKF is the assumption of Gaussian noise on the RSSI measure. The effects are limited by adopting a high standard deviation for the received RSSI, therefore $\sigma_m$ is tuned to $5dB$. All other variables in $\mathbf{R}$ can be tuned according to the expected noise in the other measurements.

The process noise matrix $\mathbf{Q}$ is the diagonal matrix presented in Equation 11. It needs to be tuned so as to define the validity of the expected process [50].

$$\mathbf{Q} = \begin{bmatrix} \sigma_{Q_p}^2 \cdot \mathbf{I_{2\times 2}} & & & \\ & \sigma_{Q_v}^2 \cdot \mathbf{I_{4\times 4}} & & \\ & & \sigma_{Q_\psi}^2 \cdot \mathbf{I_{2\times 2}} & \\ & & & \sigma_{Q_h}^2 \cdot \mathbf{I_{2\times 2}} \end{bmatrix}. \tag{11}$$

$\sigma_{Q_p}$ is the standard deviation of the process noise on the relative position update. $\sigma_{Q_v}$, $\sigma_{Q_\psi}$, and $\sigma_{Q_h}$ are the process noises for the expected updates in velocity, orientation, and height respectively. The tuning is made such that a high-level of trust is put on the relative position update, whereas lower trust is put on the update of the other quantities. This promotes convergence towards a bearing estimate and helps to discard the high noise and disturbance in the RSSI measurements. In this paper, the values are tuned to the following: $\sigma_{Q_p} = 0.1$, while $\sigma_{Q_v} = \sigma_{Q_\psi} = \sigma_{Q_h} = 0.5$, for a 1 to 5 ratio.

It is noted that the scheme proposed in this section suffers from a degenerate motion known as *rotation ambiguity* [51]. When the path of $\mathcal{R}_j$ perfectly matches the path by $\mathcal{R}_i$ in a straight line, range-only measurements remain constant and are not informative for bearing estimation. If the MAVs do not fly in formation, the probability of this event is low [51]. The same ambiguity takes place when both $\mathcal{R}_i$ and $\mathcal{R}_j$ are static — motion by at least one MAV is required.

### D. Preliminary Relative Localization Results

We performed flights with a Ladybird MAV around the fixed Bluetooth W1049B antenna in order to obtain preliminary insights of the performance of the EKF during flight, useful for designing the collision avoidance strategy proposed in Section III. An Optitrack motion-capture system [52] was used to guide the MAV and record ground-truth 3D position, velocity, and orientation. Bluetooth RSSI data was recorded from the communication between the Ladybird MAV and the antenna. All data was recorded together at a rate of $5Hz$; this is a current limitation of the Bluetooth communication set-up, later discussed in Section IV.

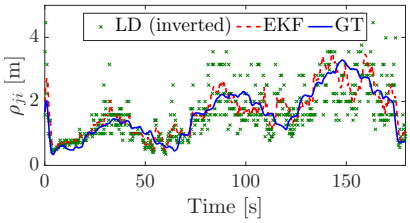


(a) Estimated range (red, dashed) between Ladybird MAV and Bluetooth antenna compared to ground truth (blue, solid) and estimate from inverting the LD model (green, dotted).

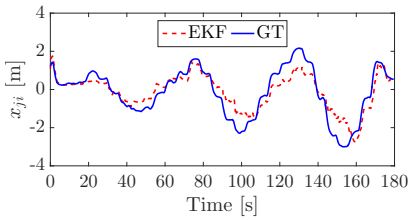


(b) Estimated (red, dashed) relative location of the Ladybird MAV along the $x_B$-axis of the antenna compared to ground truth (blue, solid).

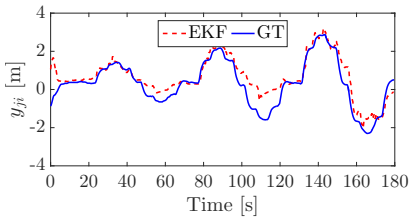


(c) Estimated (red, dashed) relative location of the Ladybird MAV along the $y_B$-axis of the antenna compared to ground truth (blue, solid).

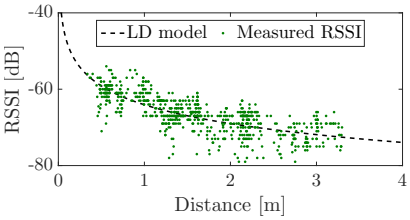


(d) Measured RSSI (green, dotted) at different ranges and the LD model used (black, dashed). The parameters of the LD model are: $P_n = -63$ and $\gamma_l = 2.0$.

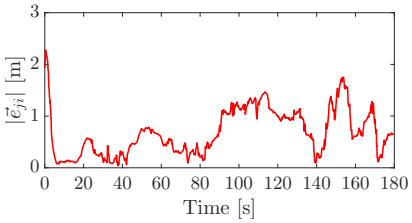


(e) Magnitude of pose error over time. Notice the convergence of the error in the initial seconds.

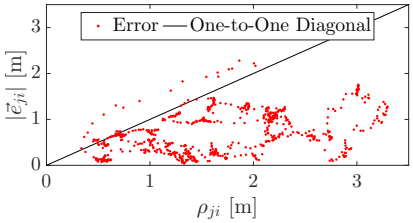


(f) Positive correlation between magnitude of pose error and distance below a diagonal line. The errors seen above the diagonal line are from the initial seconds prior to convergence.

Fig. 3: Preliminary localization results based on circular flights of a Bluetooth equipped Lisa-S Ladybird MAV around a fixed antenna. These results have been averaged over 50 iterations of artificial noise added to the velocity, height, and orientation measurements.

The data gathered was used to process the EKF off-board. The recorded velocity and orientation data from Optitrack was altered with Gaussian noise and used as measurements for the EKF. This simulated the measurement of these values using on-board sensors. The standard deviation of the noise given to velocity measurements is $\sigma_v = 0.2m/s$. The standard deviation of the noise given to altitude measurements is $\sigma_h = 0.2m$. The standard deviation of the noise given to orientation measurements is $\sigma_\psi = 0.2rad$. These values were also included in the measurement noise matrix $\mathbf{R}$. In the LD model of the EKF: $P_n = -63dB$ and $\gamma_l = 2.0$, assuming free-space propagation.

Figure 3 shows the results of the relative localization estimates achieved by the EKF. The antenna is $\mathcal{R}_i$ and it is trying to localize the MAV $\mathcal{R}_j$. The top row shows the output of the EKF against Ground-Truth (GT) data. An immediate benefit observed is the significant reduction in error for the observed range, see Figure 3a. Estimates for $x_{ji}$ and $y_{ji}$ are shown in Figure 3b and Figure 3c. Let $\vec{e}_{ji}$ be the error in pose between the estimated position of $\mathcal{R}_j$ and the real position of $\mathcal{R}_j$ with respect to $\mathcal{F}_{B_i}$ (for a visual representation, see Figure 4). $|\vec{e}_{ji}|$, the magnitude of $\vec{e}_{ji}$, is shown over time in Figure 3e. Of particular interest for the subsequent development of a collision avoidance strategy is the observed increase of this error with the distance, as seen in Figure 3f. The increase is explained by the logarithmic relationship between RSSI and distance. The diagonal (one-to-one) line in Figure 3f indicates a maximum accepted error magnitude. When $|\vec{e}_{ji}|$ is above the line, then the error encompasses the position of $\mathcal{R}_i$ itself, rendering it insufficient to select an appropriate maneuver for collision avoidance. In the results, this is only observed for data over the first few seconds of flight prior to the convergence of the EKF.

## III. COLLISION AVOIDANCE BEHAVIOR

This section describes the devised planar collision avoidance algorithm. It is based on the Collision Cone (CC) framework [53], adjusted to suit the errors and short-comings of the relative localization algorithm. The general avoidance scheme is described in Section III-A and Section III-B. Some remarks regarding its similarities and differences to other avoidance strategies found in literature are given in Section III-C.

### A. General Avoidance Strategy

A CC is a set of all velocities of an agent that are expected to lead to a collision with an obstacle [53]. Consider once more MAVs $\mathcal{R}_i$ and $\mathcal{R}_j$. We can then define a set $CC_{ji}$ that includes all velocities of $\mathcal{R}_i$, defined in $\mathcal{F}_{B_i}$, which could lead to a collision with $\mathcal{R}_j$.

Collision cones are so called because they are geometrically cone-shaped. Figure 4 depicts a collision cone $CC_{ji}$. It is constructed using Equation 12 to Equation 14 as follows. First, a general cone $CC_{ji}$ is defined as in Equation 12. $\alpha$ is an angle in radians, and $x$ and $y$ are points on $x_{B_i}$ and $y_{B_i}$, respectively. The cone is characterized by an expansion angle

$\alpha_{CC_{ji}}$, expressed in radians and subject to $0 < \alpha_{CC_{ji}} < \pi$.

$$CC_{ji} = \{(x,y) \in \mathbb{R}^2; \alpha \in \mathbb{R}; |\alpha| \leq \frac{|\alpha_{CC_{ji}}|}{2} : \tan(\alpha)x = y\} \tag{12}$$

Then, the cone is rotated so as to be centered around the estimated bearing to the obstacle $\mathcal{R}_j$ as in Equation 13, where: $\bar{\beta}_{ji}$ is the estimated $\beta_{ji}$, $\leftarrow$ is an update operator, and $\mathbf{R}(\cdot)$ is a rotation operator for the set.

$$CC_{ji} \leftarrow \left(\mathbf{R}(\bar{\beta}_{ji}) \cdot CC_{ji}\right) \tag{13}$$

Finally, the entire cone is translated by the estimated velocity of $\mathcal{R}_j$ expressed in $\mathcal{F}_{B_i}$, to account for the fact that the obstacle is moving, as per Equation 14. $\overline{\dot{\vec{p}}_{jRi}}$ is the estimated $\dot{\vec{p}}_{jRi}$. The operator $\oplus$ denotes the translation of a set by a vector (for instance, $S \oplus \vec{s}$ indicates the translation of set S by vector $\vec{s}$) [53].

$$CC_{ji} \leftarrow CC_{ji} \oplus \overline{\dot{\vec{p}}_{jRi}} \tag{14}$$

Estimates of $\beta_{ji}$ and $\dot{\vec{p}}_{jRi}$ are extracted from the EKF proposed in Section II. If exact estimates were available, $\alpha_{CC_{ji}}$ would only be dependent on the radii of the two MAVs (modeled as circular objects) [30]. Errors may be accounted for by increasing $\alpha_{CC_{ji}}$ [20]. In the following, we propose a method to establish the expansion angle tailored to the errors of the Bluetooth relative localization scheme.

In Figure 3f it is observed that the magnitude of the localization error increases with the distance, extrapolated to the following relationship:

$$E(|\vec{e}_{ji}|) = \frac{1}{\kappa_\alpha} \cdot \bar{\rho}_{ji}, \tag{15}$$

where $\kappa_\alpha$ is a constant coefficient describing the quality of the estimate. $E(\cdot)$ is the expected value. $\bar{\rho}_{ji}$ is the estimated range between $\mathcal{R}_i$ and $\mathcal{R}_j$. Note that if $\kappa_\alpha < 1$ then $E(|\vec{e}_{ji}|) > \bar{\rho}_{ji}$, meaning that the potential bearing estimation error is $2\pi$ and it does not provide useful information for collision avoidance. If $\kappa_\alpha \geq 1$, then the estimate is sufficiently accurate to select a collision escape trajectory. In Figure 3f we observed that errors after the initial convergence convergence are below the diagonal line of $\kappa_\alpha = 1$. In this paper, we take this worst-case scenario and *select* $\kappa_\alpha = 1$. We then define the expansion angle $\alpha_{CC_{ji}}$ based on the implication of $E(|\vec{e}_{ji}|)$ on the bearing error with Equation 16:

$$\alpha_{CC_{ji}} = 2 \cdot \tan^{-1}\left(\frac{\bar{\rho}_{ji} + r_i + r_j + \varepsilon_\alpha}{\kappa_\alpha \cdot \bar{\rho}_{ji}}\right). \tag{16}$$

$r_i$ and $r_j$ are the radii of the MAVs. In a homogeneous team: $r_i = r_j$. $\varepsilon_\alpha$ is an additional margin, the properties of which are discussed in Section III-B. $\alpha_{CC_{ji}}$ is subject to an asymptote on its lower limit as $\bar{\rho}_{ji} \to \infty$. Its impact may be appreciated in Figure 5. The asymptote (denoted $\alpha_{CC_{asymptote}}$) is dependent on the selected value of $\kappa_\alpha$:

$$\alpha_{CC_{asymptote}} = \lim_{\bar{\rho}_{ji}\to\infty} \alpha_{CC_{ji}} = 2 \cdot \tan^{-1}\left(\frac{1}{\kappa_\alpha}\right). \tag{17}$$

In this work, $\kappa_\alpha$ is selected as 1. The asymptote of the expansion angle is thus $\pi/2$.

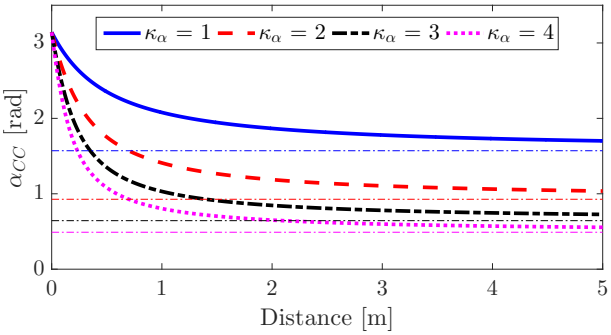


Fig. 5: Effect of $\kappa_\alpha$ on $\alpha_{CC}$ along distance $\rho_{ji}$. The other parameters are set to $r_i = r_j = 0.1m$ and $\varepsilon_\alpha = 0.5$. The straight lines represent the relevant asymptotes.

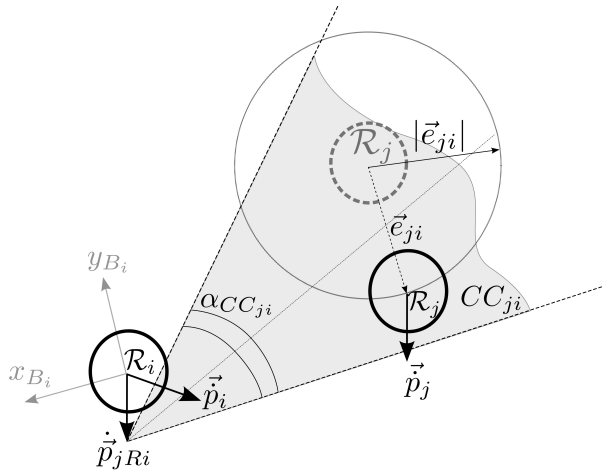


Fig. 4: Depiction of $CC_{ji}$ that $\mathcal{R}_i$ holds with respect to $\mathcal{R}_j$. The dashed circle is the estimated location of $\mathcal{R}_j$. $\vec{e}_{ji}$ is the localization error. $\alpha_{CC_{ji}}$ is the *expansion angle* of the cone.

In a team of $m$ MAVs, each member $\mathcal{R}_i$ holds $m-1$ collision cones that it can superimpose into a single set $CC_i$:

$$CC_i = \bigcup_{j=1}^{m-1} CC_{ji} \tag{18}$$

If, during flight, $\vec{p}_i \in CC_i$, then a *clock-wise* search about the $z_{B_i}$ axis (starting with the current direction of flight) is used to determine the desired velocity for escape from a collision course. The clock-wise search aims to hold the nominal desired magnitude for $\vec{p}_i$. If no solution is found, then the search is repeated for a higher escape speed.

### B. Preserving Behavior in Different Room Sizes

Equation 16 does not generalize well to environments of different sizes when all its parameters ($r_i$, $r_j$, $\kappa_\alpha$, $\varepsilon_\alpha$) remain constant. Too small values of $\kappa_\alpha$ and/or too large values of $\varepsilon_\alpha$ can enlarge the collision cone too much and restrict freedom

of movement when operating in smaller rooms. This brings two separate disadvantages, both in part culprits for eventual collisions:

1) Oscillations/instability in MAV trajectories;
2) Convergence of the EKF suffers due to small noise-like movements.

Appropriate scaling of the collision cone is achieved by altering $\varepsilon_\alpha$, which dictates the slope for the change in $\alpha_{CC}$ at smaller distances, see Figure 6.

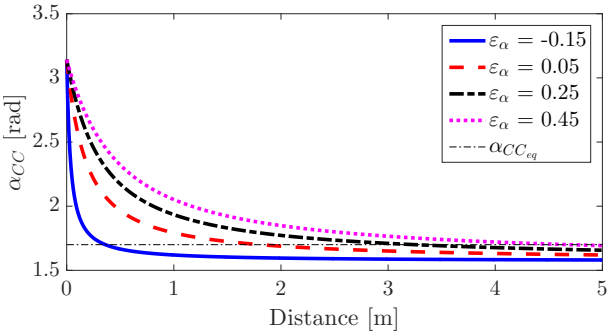


Fig. 6: Effect of $\varepsilon_\alpha$ on $\alpha_{CC}$ along $\rho_{ji}$. The other parameters are set to $r_i = r_j = 0.1m$ and $\kappa_\alpha = 0.5$.

By re-arranging Equation 16, $\varepsilon_\alpha$ can be determined with the following rule:

$$\varepsilon_\alpha = \kappa_\alpha \cdot \rho_{eq} \cdot \tan\left(\frac{\alpha_{CC_{eq}}}{2}\right) - (r_i + r_j) - \rho_{eq}, \qquad (19)$$

This equation relies on the pair of parameters $\rho_{eq}$ and $\alpha_{CC_{eq}}$. $\alpha_{CC_{eq}}$ is the desired angle of expansion at a distance $\rho_{eq}$. For a given $\kappa_\alpha$, $\varepsilon_\alpha$ can be adjusted with Equation 19 to adapt the expansion of the cone when $\rho_{eq}$ changes. Note that $\alpha_{CC_{eq}} > \alpha_{CC_{asymptote}}$. Equation 19 sets the limit $\varepsilon_\alpha \geq -(r_i + r_j)$ if $\kappa_\alpha \geq 1$.

The selection of $\rho_{eq}$ and $\alpha_{CC_{eq}}$ is left to the designer based on the expected circumstances. Due to the conservative choice of $\kappa_\alpha$, lower values of $\rho_{eq}$ would be preferred to enable mobility. In all tests in this article, $\rho_{eq}$ is at a distance that is half of the expected side length of the (square) arena. $\alpha_{CC_{eq}}$ is kept at a $1.7rad$. In a realistic adaptive task, under the assumption that the MAVs are equipped with a wall-sensor, then they could define $\rho_{eq}$ on-board based on the distance to the surrounding walls.

### C. Connection with Velocity Obstacle Methods

One may note the resemblance of the proposed avoidance strategy to the Velocity Obstacle (VO) method. The difference is that VO selects a new flight direction that minimizes the required change in velocity [30] [31] as opposed to the clockwise search suggested here. VO is notoriously prone to *reciprocal dances* [54]. These are oscillations in the trajectory when entities heading towards each-other repeatedly select the same escape direction, leading to a left-right "dance". Reciprocal dances arise when each entity (wrongly) assumes that the other will not change its course and avoidance will not be reciprocal. Several variants attempt to solve this issue by making the opposite assumption, i.e. that both entities will try to evade the collision. Examples include Reciprocal Velocity Obstacle (RVO) [55], Hybrid Reciprocal Velocity Obstacle (HRVO) [56] [57], and Optimal Reciprocal Collision Avoidance (ORCA) [58]. In our case, however, due to the potential for large relative localization errors, the MAVs are not made to assume that the others will participate in a suitable and reciprocal escape maneuver. Reciprocal variants of VO are thus discouraged and reliance on own estimates and avoidance is preferred. The clockwise search encourages a preference for right-sided maneuvers with respect to the current flight direction, automatically resolving reciprocal dances.

## IV. TEST SET-UP

This section describes the tests that have been set up to establish the performance of the combined system in a realistic team flight. This has first been done in simulation in order to establish the limitations, and later in the real-world, with the different objective of establishing the reality gap resulting from the use of real RSSI measurements and real on-board velocity estimates for data exchange between MAVs.

### A. Description of Arbitrary Task for Performance Testing

A controller is designed to instantiate an arbitrary task and applied homogeneously to all MAVs. The task is designed such that the MAVs repeatedly seek to pass *through* the center of the arena. This is made so as to provoke several potential collision scenarios and observe if/how these scenarios are resolved.

Consider a team of $m$ homogeneous MAVs. Each MAV $\mathcal{R}_i$ is controlled in velocity. Let $\vec{p}_{i_{cmd,k}}$ be the desired velocity for $\mathcal{R}_i$ expressed in its body-frame $\mathcal{F}_{B_i}$ at a given time-step $k$. Let $d_{wall_i}$ be the distance between $\mathcal{R}_i$ and the arena border that is closest to it, with $d_{safe}$ being a safety distance to the arena's borders. Remember that each robot $\mathcal{R}_i$ features $m-1$ EKF instances to keep track of the other members and uses their outputs to determine its collision cone set $CC_i$, see Equation 18. At each-time step $k$, the EKF outputs are updated and $CC_i$ is re-calculated. $\vec{p}_{i_{cmd,k}}$ is then chosen as follows: $\dot{\vec{p}}_{i_{cmd,k}} = \dot{\vec{p}}_{i_{cmd,k-1}}$ unless conditions M1 and M2 take place.

M1: $d_{wall_i} < d_{safe}$ and $\dot{d}_{wall_i} < 0$. This means that $\mathcal{R}_i$ is close to the arena border and approaching it. Then, $\dot{\vec{p}}_{i_{cmd,k}}$ is rotated towards the center of the arena. See Figure 7.

M2: $\dot{\vec{p}}_i \in CC_i$. This means that the current velocity of $\mathcal{R}_i$ could lead to a collision with one or more team members. An escape velocity is sought according to the strategy proposed in Section III.

Note that M1 supersedes M2 to ensure that the MAVs remain within the confines of the arena. At all time-steps, unless other-wise commanded by the collision avoidance algorithm, $|\dot{\vec{p}}_{i_{cmd,k}}| = v_{nominal}$, where $v_{nominal}$ is a fixed speed magnitude. The MAVs fly at the same height at all

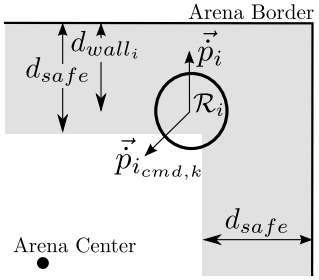


Fig. 7: Depiction of MAV $\mathcal{R}_i$ subject to condition M1 at a time step $k$. $\mathcal{R}_i$ is closer to the arena border than $d_{safe}$ allows, and moving towards it (see its velocity, $\dot{\vec{p}}_i$). When this happens, the commanded velocity ($\vec{p}_{i_{cmd,k}}$) is oriented towards the center of the arena.

times.

The controller described above is implemented as a call-back function upon the reception of new data from other MAVs. This runs at $5Hz$ due to the limitations of the real-world implementation (see Section IV-D). Furthermore, the MAVs always maintain the same heading with respect to North, purposely taking advantage of the 6-Degrees of Freedom (DOF) dynamics of quadrotors. In all experiments $v_{nominal} = 0.5m/s$. In all simulations $d_{safe} = 0.25m$. In all real-world tests, for conservative/safety reasons, $d_{safe}$ was increased to $0.5m$.

Section IV-C and Section IV-D describe the implementation of the above in the simulation environment and the real-world, respectively. At this early research stage, it will be noticed that both implementations equally rely on an external position sensor in order to enforce M1. In a real-world task, arena borders would be detected using environment features such as walls (e.g. [59]) and the center of the arena would represent an attraction way-point.

In all instances, the MAVs begin the task at different corners of the arena (this is approximate for the real-world tests). The EKF is initialized such that the initial position estimate is towards their initial flight direction (i.e. approximately the center of the arena). All other states are initialized as null. The covariance matrix of the EKF is initialized as an identity matrix.

### B. Testing Several Density Configurations

The performance of the task described in Section IV-A is dependent on how crowded/dense the airspace is. This has been investigated by altering both arena size and MAV diameter in different configurations. The investigated configurations and their respective densities are shown in Table 8. These will be referred to throughout the remainder of this article by the numbers in the circles.

Airspace density is calculated by modeling each MAV as a circle in a square arena. Let $\mathcal{D}_{m,c}$ denote the density

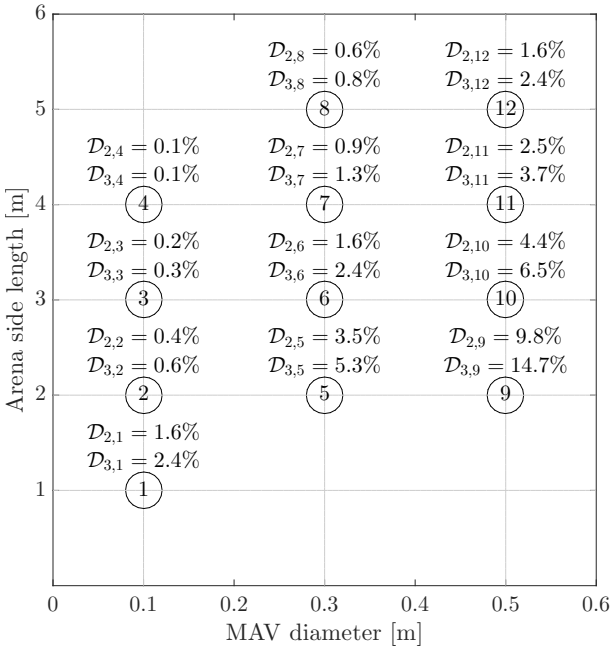


Fig. 8: Matrix graph of all configuration pairs of MAV diameter and side length of square arena considered for testing. The configuration numbers (shown in the white circles) are referenced throughout the remainder of this article. $\mathcal{D}_{m,c}$ is the airspace density for configuration $c$ when featuring a team of $m$ MAVs.

for configuration $c$ with $m$ MAVs. It is calculated as in Equation 20.

$$\mathcal{D}_{m,c} = \frac{m \cdot \pi r_c^2}{s_c^2} \tag{20}$$

$r_c$ is the radius of an arbitrary MAV at configuration $c$ (all MAVs in a configuration are homogeneous). $s_c$ is the side length of the squared arena at configuration $c$. Tests were performed with two MAVs ($m = 2$) and three MAVs ($m = 3$).

### C. Simulation Environment Set-Up

The simulation environment was built using the Robotics Operating System (ROS) [60]. It adopts the *Gazebo* physics engine [61] and the *hector-quadrotor* [62] simulation which together provide a validated platform. [1] Multiple instances of a quad-rotor may be launched in a simulation run. The core functions (i.e. relative localization EKF and collision avoidance controller) are developed for and within Paparazzi Unmanned Air Vehicle (UAV) software [63] [64] [2]. This is so as to be readily portable to the real-world set-up described in Section IV-D. A ROS module (a.k.a. "node" [60]) for each MAV simulates the presence of a Bluetooth RSSI sensor and subsequently enforces the controller

[1] At the time of writing: ROS is freely available at `www.ros.org`; Gazebo is freely available at `www.gazebosim.org`; Hector-quadrotor is freely available at `wiki.ros.org/hector_quadrotor`.

[2] Paparazzi UAV is an open-source UAV/MAV auto-pilot software available at `https://github.com/paparazzi/paparazzi`.

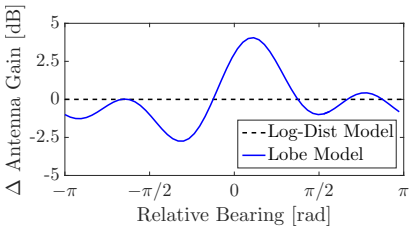


(a) Lobes applied to the simulated RSSI signals on each simulation. The lobes superimpose as elaborated in [11].

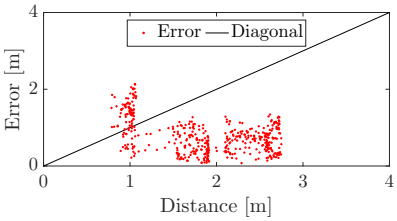


(b) Localization error over simulation of a concentric circular flight about a static antenna The higher errors at 1m are prior to the convergence of the EKF.

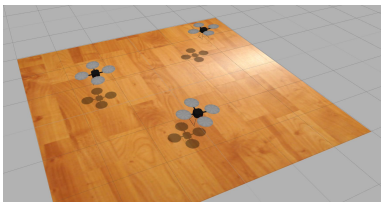

(c) Gazebo visualization of a simulation with 3 MAVs.

Fig. 9: Figures relating to the development of the Gazebo/ROS simulation environment.

described in Section IV-A. The module runs at $5Hz$ to match the communication speed between MAVs achieved in the real-world (see Section IV-D).

The RSSI signal was simulated using the LD model ($P_n = -63dB$, $\gamma_l = 2.0$) with added Gaussian noise as well as horizontal lobes as a function of relative bearing. The standard deviation of the added noise, with the exception of the results discussed in Section VI-C, is $5dB$. The lobes were arbitrarily modeled using a third order Fourier series with unitary weights, see Figure 9a. The other measurements were altered with the same standard deviations as in the preliminary tests of Section II-D. With Figure 9b, we see that the achieved performance of the simulated on-board relative localization scheme features similar error magnitudes as observed in Figure 3e when a similar test is repeated in simulation.

Each configuration from Table 8, unless otherwise stated, has been tested with 100 trials featuring a maximum trial time of $500s$ for two MAVs and three MAVs. The simulations are interrupted whenever the actual distance between any two MAVs is smaller than the sum of their radii, indicating a collision. A screen-shot of a simulation with 3 MAVs is shown in Figure 9c.

### D. Real-World Environment Set-Up

We executed real-world experiments using AR-Drones 2.0 [65] running Paparazzi. The drones all flew at $1.5m$ above the ground within a $4m \times 4m$ arena. Figure 10 shows a picture of an on-going experiment with 3 drones.

A BLED112 Bluetooth Smart USB Dongle was used to provide the AR-Drones with Bluetooth 4.0 capabilities [66]. All computations for relative localization and collision avoidance are run on-board of the AR-Drones. The LD model in the EKF filter was given: $P_n = -67dB$ and $\gamma_l = 2.0$. $P_n$ was obtained by a brief hand-held calibration measurement. The choice of $\gamma_l$ was based on the free-space assumption [34]. Communication between the AR-Drones was *direct* via Bluetooth. The data was sent and received by means of advertising messages scheduled using a Self-Organized Time Division Multiple Access (STDMA) algorithm [67]. Under the STDMA algorithm, each MAV's Bluetooth antenna alternates between advertising and listening, achieving data exchange at a rate of $5Hz$. This enabled direct communication circumventing the Master-Slave paradigm otherwise enforced by the Bluetooth standard [68].

Fig. 10: Picture during a real-world experiment with 3 AR-Drones 2.0 (encircled in white) inside the arena.

Two different real-world tests were performed. Test #1 explored the impact of using real RSSI measurements and communication. Test #2 then explored the effect of using on-board velocity estimates. The two tests are described in more detail in the next two paragraphs.

*Test #1 (Optitrack-based state estimation):* The primary objective of this test was to establish the performance of the relative localization and collision avoidance algorithm when using real RSSI measurements and Bluetooth communication. On-board state estimation of velocity, magnetic North orientation, and height was purposely avoided in order to be able to ensure regulated noise and isolate the impact of using real Bluetooth RSSI. Optitrack [52] was used to provide the MAVs with estimates of their *own* states via a Wi-Fi link. These were artificially altered with Gaussian noises $\sigma_v = 0.2m/s$ and $\sigma_\psi = 0.2rad$ upon being entered into the EKF. Furthermore, Optitrack position data was used to guide MAVs according to condition M1 as proposed in Section IV-A. The enforced arena size in all experiments was $4m \times 4m$. These experiments are approximately analogous to Configuration 11 from

the simulated tests (AR-Drones 2.0 are slightly larger in diameter than $0.5m$). Experiments were performed with both two AR-Drones and three AR-Drones.

*Test #2 (On-board velocity estimation):* These tests were performed using two AR-Drones. The objective was to determine the impact of using realistic velocity sensors on the relative localization performance and its repercussions on collision avoidance. Instead of relying on Optitrack, the AR-Drones estimated their own velocity using on-board sensors and the the Optical Flow module available within Paparazzi [3]. The on-board estimates were then directly communicated between the AR-Drones using Bluetooth. For safety reasons, and to isolate the impact of the relative localization estimate on collision avoidance, on-board velocity estimates were *only* used as inputs for the EKF relative localization. The velocity controller of the AR-Drones remained reliant on Optitrack. This ensured controlled flight within the confines of the arena. The drones kept a constant heading towards North and the same height at all times. No noise was artificially added to the velocity measurements. All other parameters remained as in Test #1.

## V. RESULTS

### A. Simulation Results

All configurations presented in Section IV-B have been tested under the simulation environment described in Section IV-C. The objective of the simulations is to study the performance trends under different environments and the limitations of the system. The parameter used to assess the performance is the *flight-time to collision*, which is the time that the MAVs managed to fly within the arena whilst avoiding collisions. This is shown for each configuration in Figure 11. Remember that simulations were stopped after $500s$ of flight in the event of no collisions. For all configurations, flights with three MAVs show a lower performance with respect to two MAVs. In the simulations, the introduction of an additional MAV does not affect the relative localization performance between MAVs. Therefore, the performance drop is a result of the team dynamics at play, namely: 1) increased airspace density; 2) decreased freedom of movement due to superposition of collision cones. These two factors are analyzed in the remainder of this section.

When the arena side length remains constant and the MAV diameter increases, a decrease in mean flight-time is systematically present. This is observed when comparing within the configuration triads 4-7-11, 3-6-10, and 2-5-9, and the pair 8-12. The result is analogous when MAVs of the same diameter are used in arenas of different sizes, as may be noticed by observing the configuration quartets 1-2-3-4, 5-6-7-8, and 9-10-11-12. This implies that a lower density improved the probability of success, but this is found to not strictly be the case. Figure 12a shows the flight

[3]See the module *computer_vision/opticflow* for a more in-depth description. It is noted that this module is under active development.

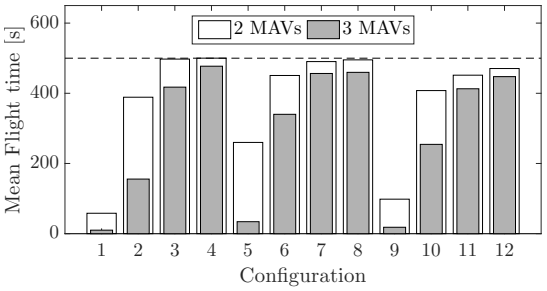


Fig. 11: Mean flight-time to collision for all configurations with active collision avoidance. The maximum simulation time for each trial was $500s$ in the event of no collisions. The mean flight times without collision avoidance, not seen in this figure, range between $3.9s$ and $14.3s$.

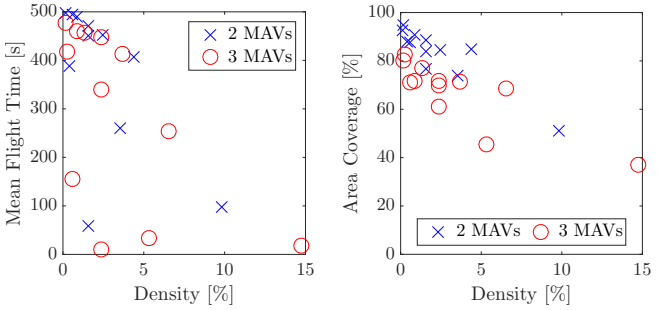


(a) Mean flight-time with respect to density

(b) Mean area-coverage with respect to density

Fig. 12: Flight parameters with respect to airspace density based on simulation results.

time to collision as a function of the airspace density. A portion of configurations show low results in spite of the low airspace density, and are outliers in the negative linear trend. These correspond to configurations 1, 2, 5, and 9, which feature smaller arena sizes. The conclusion is that room size affects performance even when airspace density remains constant. This is a limitation of the current status of the system when operating in smaller room sizes. Its causes are discussed in Section VI-B.

Figure 12b shows the impact of airspace density on area coverage for all flights with two MAVs and three MAVs. Area coverage is measured as follows. The arena is divided in sections. A section is then considered covered if at least one of the MAVs crosses it during a trial. Area coverage is the ratio of covered sections to the total number of sections. The calculation was performed using standardized sections of $0.20m \times 0.20m$. Two patterns are discerned. The first is the general trend that a higher airspace density leads to a lower overall coverage. This is a combined effect of a) lower flight times, providing less opportunity for movement, and b) decreased freedom of movement due to larger portions of the arena being covered by collision cones. The second pattern is that flights with three MAVs systematically achieve lower area coverage if compared to flights with two MAVs at the same density. This is explained

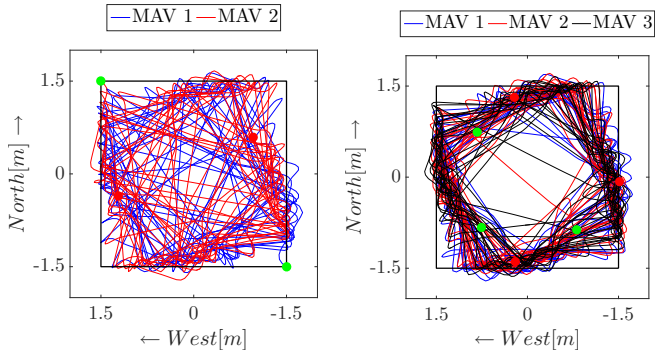


(a) Emergent circular trajectory with two MAVs.

(b) Emergent circular trajectory with three MAVs.

Fig. 13: Trajectories from two exemplary simulated flights of $500s$ extracted from configuration 10 showing the emergent circular behavior with two MAVs (left) and three MAVs (right). The starting positions are shown in green (note that for the flight with three MAVs this was actually at the corners, but the first few time-steps were not logged). The final positions are shown in red.

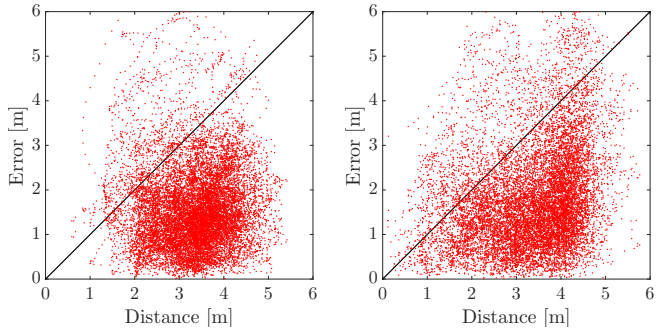


(a) Localization error magnitude for all flights two AR-Drones in Test #1.

(b) Localization error magnitude for all flights three AR-Drones in Test #1.

Fig. 14: Overview of magnitude of relative position estimate error ($|\vec{e}_{ji}|$ between all MAVs during all flights with two AR-Drones (left) and three AR-Drones (right). All data shown here equally relied on off-board self-state estimates (Test #1).

by analyzing the flight trajectories in more detail, which show an emergent circular behavior. This behavior may be appreciated in Figure 13, showing two exemplary runs from a simulation with two (Figure 13a) and three (Figure 13b) MAVs from configuration 10. When more than one MAV to avoid is present, the superposition of multiple collision cones significantly discourages the pursuit of the desired trajectory. The result is clock-wise motion along the sides of the arena for all MAVs. Oscillations along the border are observed as conditions M1 and M2 alternate.

### *B. Real-World Results with Optitrack-based State Estimation (Test #1)*

Four flights were performed with two AR-Drones in a $4m \times 4m$ arena. The cumulative flight-time was $25.3min$. In this time, the MAVs only suffered from one collision, which took place in the second flight after $5.6min$. The other flights lasted $6.1min$, $7.6min$, and $6.0min$; they were ended manually in order to preserve battery health in light of low battery voltage.

Six flights were performed with three AR-Drones for a cumulative time of $15.3min$. Five out of six flights ended due to collisions. The flights ending with collisions reached a mean flight time of $160s$ ($2.7min$) before ending with collisions. The shortest flight was $33s$, the longest flight was $5.2min$. The other flights lasted $1.9min$, $2.6min$, and $3.0min$. The flight without a collision was manually ended after $2.0min$ due to low battery voltage. Under these results, a system with three MAVs can expect a collision once every $184s$ ($\approx 3min$) of flight under the proposed task.

Figure 14 shows the magnitude of the localization error ($|e_{ji}|$) for all combinations and during all flights together with two AR-Drones (Figure 14a) and three AR-Drones (Figure 14b) in Test #1. For all flights with two AR-Drones, $92\%$ of all estimates are below the expected line of $\kappa_\alpha = 1$. The minimum performance by an MAV over a flight is $84.8\%$, and the maximum is $97.6\%$. For all flights with three AR-Drones, $84\%$ of points are below the expected line.

Figure 15 shows the errors in bearing and range for all relative estimates during all flights. For flights from Test #1: the range error is shown in Figure 15a and Figure 15b, and the bearing error is shown Figure 15d and Figure 15e. The mean error with two MAVs features a Root Mean Squared Error (RMSE) of $0.57rad$ for bearing estimates and $0.86m$ for range estimates. With three MAVs, the RMSE rises to $0.70rad$ and $1.14m$ for bearing and range estimates, respectively.

Of particular interest is the amount of times that the bearing error temporarily diverges towards $\pm\pi$. In spite of the shorter cumulative flight time, this error case is more frequent in the flight with three MAVs. The error does not necessarily lead to collisions in light of the homogeneous application of the controller to all MAVs and the abstinence from assuming reciprocity in the collision avoidance. Nevertheless, it does introduce a temporary uncertainty in the system that is not accounted for by the collision avoidance. Furthermore, the convergence rate for bearing estimates over flights with three AR-Drones is worse than with two AR-Drones. This may be appreciated in Figure 16, which shows the first $30s$ of Figure 15d and Figure 15e in more detail. Convergence times for flights with three MAVs reach up to $30s$ prior to settling (Figure 16b). By comparison, the convergence in flights with two AR-Drones only (Figure 16a) is found to be at most within $5 - 10s$.

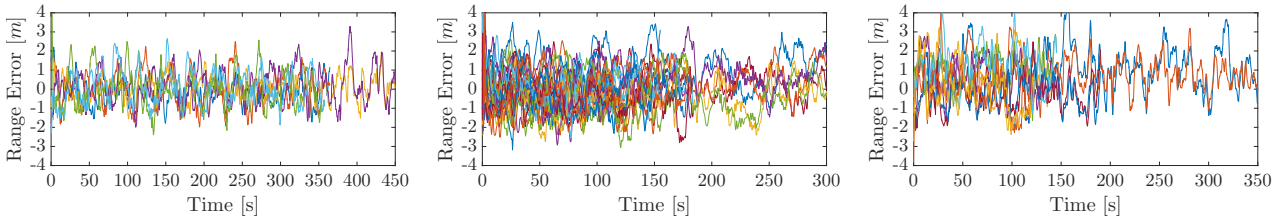


(a) Overview of range estimate error during all flights with two AR-Drones with Optitrack-based state estimation (Test #1). The RMSE is $0.86m$.




(b) Overview of range estimate errors during all flights with three AR-Drones with Optitrack-based state estimation (Test #1). The RMSE is $1.14m$.




(c) Overview of range estimate errors during all flights with two AR-Drones with on-board velocity estimation (Test #2). The RMSE is $1.18m$.

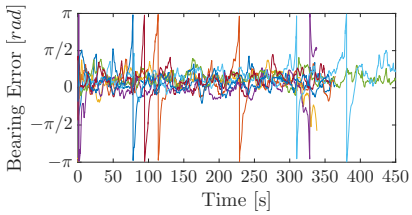


(d) Overview of bearing estimate errors during all flights with two AR-Drones with Optitrack-based state estimation (Test #1). The RMSE is $0.57rad$.

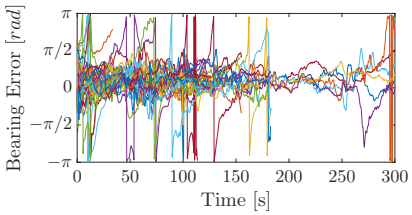


(e) Overview of bearing estimate errors during all flights with three AR-Drones with Optitrack-based state estimation (Test #1). The RMSE is $0.70rad$.

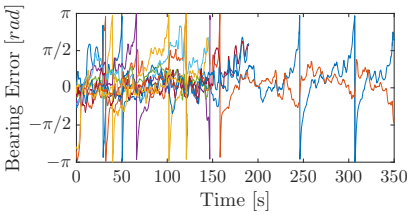


(f) Overview of bearing estimate errors during all flights with two AR-Drones with on-board velocity estimation (Test #2). The RMSE is $0.77rad$.

Fig. 15: Overview of all relative range (top) and relative bearing (bottom) errors. All plots on the left relate to flights with two AR-Drones with Optitrack-based state estimation (Test #1). All plots in the middle relate to flights with three AR-Drones with Optitrack-based state estimation (Test #1). All plots on the right relate to flights with two AR-Drones with on-board velocity estimation (Test #2).

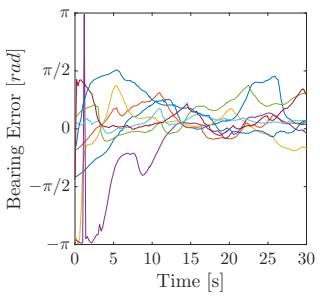


(a) Bearing error for all flights with two AR-Drones in the first $30s$.

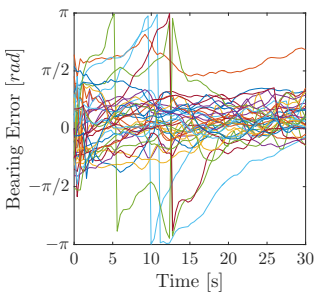


(b) Bearing error for all flights with three AR-Drones in the first $30s$.

Fig. 16: Comparison of bearing estimate errors between all performed flights with two AR-Drones (left) and three AR-Drones (right) in the first 30 seconds of flight. All data shown here equally relied on off-board self-state estimates.

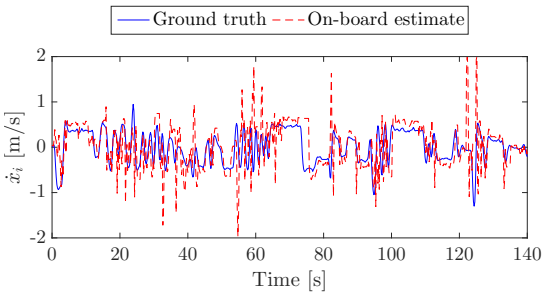


Fig. 17: Velocity estimation (red, dashed) of an AR-Drone along the $x_B$ axis against ground truth velocity (blue, solid). Notice the small spikes between $30s$ and $40s$ and the larger spikes at $\approx$ $55s$ and $\approx$ $125s$. Furthermore, notice the occasional over/under estimation in the regions between $70s$ to $80s$ and $100s$ to $110s$.

### *C. Real-World Results with On-Board Velocity Estimation (Test #2)*

For Test #2, five flights were performed with two AR-Drones for a cumulative time of $16min$. All flights ended in collisions. The mean time to collision was $192.4s$ ($3.2min$). The longest recorded flight time was $6.0min$. The shortest flight was $2.0min$. The other flights were $2.4min$, $2.4min$, and $3.1min$. This is a significant drop in performance if compared to the flights from Test #1 with two AR-Drones. The reason is in the increased error in the relative range and bearing estimates when compared to flights with two MAVs using Optitrack velocity estimates, see Figure 15c and Figure 15f. The RMSE of the relative range estimates was $1.18m$, whereas the RMSE for relative bearing estimates was $0.77rad$.

The loss in relative localization accuracy is attributed to the disturbances present in the on-board velocity estimates. Figure 17 shows an exemplary estimate of the velocity along the $x_{B_i}$ axis by one AR-Drone during a flight. At different intervals, it may be seen that the velocity was over or under estimated for an extended period of time. Furthermore, significant spikes can be seen at $\approx 55s$ and $\approx 125s$. These spikes were manually limited to a maximum magnitude of $2m/s$, yet impose significant disturbance in the localization

estimate. Finally, the standard deviation of the error reaches $\approx 0.4m/s$. This was not accounted for in the EKF, which still assumed $0.2m/s$.

## VI. DISCUSSION

### A. Performance of Relative Localization

The flights with two AR-Drones from Test #1 returned low relative localization errors and successful collision avoidance over a prolonged flight time of $25min$ with only one collision. However, a noticeable loss in relative localization performance was measured when introducing a $3^{rd}$ MAV. The effects were longer convergence times as well as higher relative bearing/range errors that negatively impacted the performance of the collision avoidance system when compared to the simulation results. The trend is assumed to get worse with team larger than 3. A similar decrease in performance was also observed when using on-board velocity estimates. This was due to a combination of over-under estimation of velocity or occasional spikes in the measurements.

The relative localization scheme uses an EKF. This may be criticized for its reliance on a Gaussian noise driven model, which fails to provide robustness against un-modeled disturbances. Other methods such as robust [69] or adaptive [70] variants of Kalman filters, or Particle Filters (PFs) [36], could be be better suited to deal with the circumstances. However, a naive change in filter can bring increased cost in computational resources without necessarily guaranteeing a higher quality output. This is because there are a number of other limitations. One is that the logarithmic decrease in RSSI makes it intrinsically insufficient to measure changes in range at larger distances. Another limitation stems from the proposed process update equation (see Equation 8). In order to provide a general scheme and abstain from introducing more complexities in the system, it is based on the null assumption that all velocities remain constant. Improvements may come from including more complex dynamic properties in the process equation, i.e. acceleration and jerk.

To make the case that a change in filter is not *necessarily* to be associated with an improved performance, we compare the performance of the EKF to that of the Unscented Kalman Filter (UKF). The UKF is correct to a higher order [71] and does not need to be influenced by the assumption of Gaussian noise [72]. Two implementations of the UKF are used, one with distribution parameter of 2 (denoted $\text{UKF}_2$) and one with a distribution parameter of 0 (denoted $\text{UKF}_0$). $\text{UKF}_2$ incorporates Gaussian noise, whereas $\text{UKF}_0$ abstains from an initial a-priori knowledge [72]. Figure 18 shows the results for the same preliminary trial run previously discussed in Section II-D. All filters were applied to the same realization of artificial noise on the measurements and featured the same initial conditions. It may be seen that the performance is comparable. One reason is that the UKF's main strength (lack of linearization [73]) is in vain due to the low non-linearity of the process/measurement equations [74]. This may change if the process equation is altered as previously suggested. Another reason is that there is still a considerable impact from un-modeled disturbances in the environment.

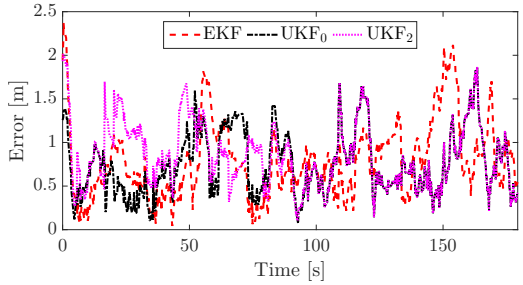


Fig. 18: Comparison of localization error ($|e_{ji}|$) with EKF (red,dashed), Gaussian UKF (purple, dotted), and non-Gaussian UKF with distribution parameter = 0 (black, dash-dotted) against ground truth data (blue, solid). The results are from one realization of artificial noise on the measurements from the same data-set used in Figure 3.

Further investigations are encouraged in order to define a filter that can lower the expected worst-case error. This would benefit the system as a whole. The collision cone parameter $\kappa_\alpha$ could be reduced without introducing additional risk. This discussion is continued in Section VI-B.

### B. Performance of Collision Avoidance

In simulation, all configurations have also been tested *without* active collision avoidance. In this case, the MAVs are only subject to condition M1. The obtained mean flight times range between $3.9s$ and $14.3s$. A $z$-test with $95\%$ confidence level [75] shows a statistically significant improvement in flight time for all configurations when using the collision avoidance method.

Figure 12a shows that an increase in airspace density is directly correlated with a decrease in performance. Smaller rooms show poorer performance than larger rooms despite similar density. The parameter $\varepsilon_\alpha$, as explained in Section III-B, implements room scaling within the collision cones. However, performance cannot reach the same levels unless the other relevant parameters (i.e. call-back rate ($5Hz$), $v_{nominal}$, $d_{safe}$, sensor noises) are also changed accordingly. Two reasons for this are:

- *The ratio of arena size to $v_{nominal}$ decreases in smaller rooms*. The rate of data exchange is $5Hz$, and this limits the decision rate of the collision avoidance controller. With other control parameters remaining constant, the relative distance traveled in smaller rooms is higher than in larger spaces.
- *Maneuver selection*. In smaller rooms, M1 has higher chances of being called due to more frequent proximity to the arena borders.

Collisions during real-world flights with three MAVs occurred along the edges of the arena. This is also observed

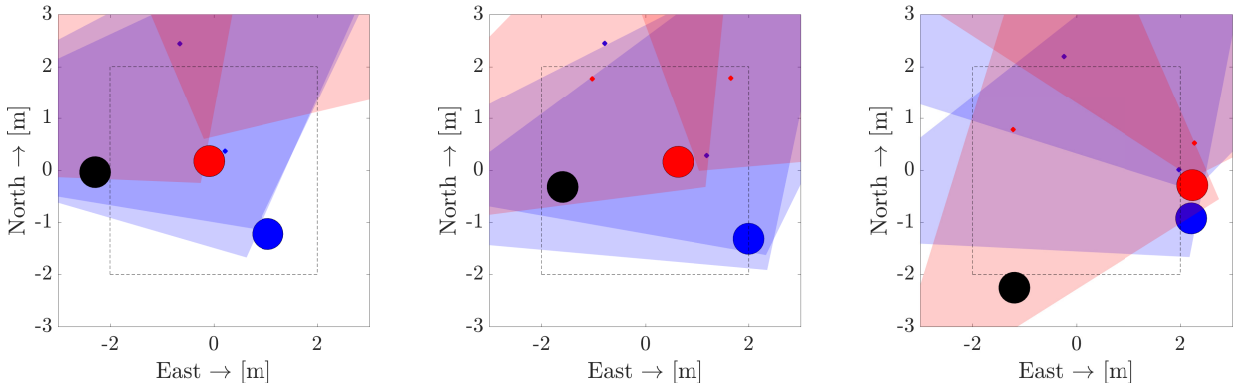


(a) View #1. The blue AR-Drone (bottom right) moves towards the right. The red AR-Drone (middle) turns away from the black MAV and also towards the right.

(b) View #2. The blue AR-Drone is trapped in the bottom right corner. The red AR-Drone continues towards the right.

(c) View #3. The blue and red AR-Drones are both trapped at the right edge of the arena and begin alternately invoking M1 and M2 (see Section IV-A). This ends with a collision.

Fig. 19: Chronological depiction (left to right) of a collision case in a real-world flight with 3 AR-Drones. Large circles indicate the ground-truth position in the arena. The collision cones of the blue and the red MAVs are shown. The blue and red diamonds indicate the current estimates by the blue and the red MAV, respectively.

in simulation. For configuration 11, $81\%$ of the collided simulated flights with three MAVs ended within $0.5m$ of the arena borders. By comparison, only $35\%$ of collided flights with two MAVs ended within this space. An example from a real-world flight is shown in Figure 19, recounted by the three events below.

1. One AR-Drone ends up "trapped" along the boundaries and is reluctant to make movements towards the center for fear of collisions. In Figure 19a we see that the bottom right AR-Drone (blue) turns towards the right.
2. Another MAV turns towards the same side. In Figure 19b, the central AR-Drone (red) avoids the black AR-Drone (on left) and also goes to the right. Its current estimate of the other trapped AR-Drone is temporarily erratic beyond the anticipated bounds.
3. The second AR-Drone also becomes "trapped" along the border. As in Figure 19c, the two oscillate along the border until a collision occurs due to proximity.

This collision scenario does not occur with two MAVs because of the larger freedom of movement and the more accurate relative location estimate.

The failure mode described above may be tackled in different ways. One option is to increase mobility by increasing $\kappa_\alpha$, prompting narrower collision cones. The results in this article are based on a conservative choice ($\kappa_\alpha = 1$) so as to account for a worst case scenario, but this could be alleviated in order to resolve these situations. However, if not accompanied by an improvement in the relative localization estimate, this can increase the risk of collision. Alternatively, the linear relationship of the error with distance from Equation 15 could be changed into a piece-wise function in order to limit growth of the collision cone beyond a certain distance. This would allow for a higher error tolerance but *only* for objects beyond a certain estimated range. For example: $\kappa_\alpha = 1$ if $\rho_{ji} \leq 3$ and $\kappa_\alpha = 2$ if $\rho_{ji} > 3$. A third option would be to implement a selective obstacle avoidance method that prioritizes between obstacles.

### C. Impact of Noise on System Performance

The real-world tests with two AR-Drones using off-board (Test #1) and on-board (Test #2) state estimation have shown how the performance of the relative localization algorithm is dependent on high-quality on-board estimates. The performance dropped from one collision in a cumulative $25min$ of flight to one every $\approx 3min$. To continue the discussion from the perspective of the RSSI measurements, this section investigates the extent to which an improvement in RSSI noise can lead to improved performance. In simulation, two case-studies are made. In the first case, the simulated RSSI noise is reduced from $5dB$ to $3dB$; lobes are still simulated. In the second case, RSSI noise is kept at $5dB$ but sensor lobes (all simulated disturbances) are removed. All EKF and collision avoidance parameters remain unchanged. The configurations analyzed are those with the lowest performance: 1, 2, 5, 6, 9, 10. The results are shown in Figure 20. It is systematically observed that removing the antenna lobes improves the performance. A lower noise also improves results, yet the impact is (generally) lower than antenna lobes. The lower error in relative position estimates successfully translates to a more successful collision avoidance system. This shows that performance could be improved further if operating in cleaner environments or if using higher quality sensors.

## VII. CONCLUSION

In real world tests using the solution proposed in this paper, two ARDrones 2.0 flying in in a $4m \times 4m$ space only collided once over a cumulative flight-time of $25min$. With three ARDrones 2.0, all else being equal, time between

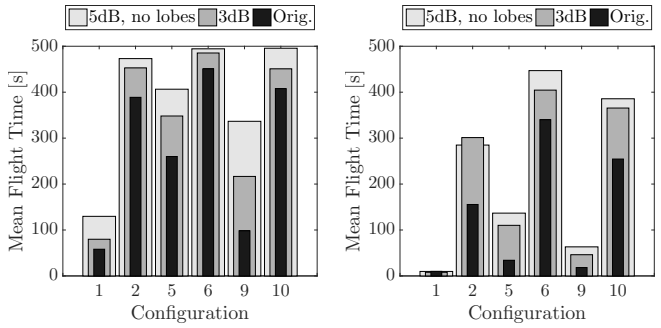


(a) Improvements in system performance with two MAVs when noise/disturbances are reduced.

(b) Improvements in system performance with three MAVs when noise/disturbances are reduced.

Fig. 20: Improvements in system performance against original results ("Orig.", black, narrowest) when noise is reduced from $5dB$ to $3dB$ (dark gray, mid width) or when lobes are removed (dark gray, widest). The left figure is for a system with two MAVs and right figure is for a system with three MAVs. For configuration properties, refer to Table 8.

collisions was $\approx 3min$. When the AR-Drones were made to estimate their own velocity on-board using optical flow, two AR-Drones collided approximately every $3min$ as a result of the disturbances in the on-board velocity estimate. Simulation trials have shown that smaller MAVs in the same space would generally lead to lower collision rates.

The combined relative localization/collision avoidance system as presented and tested in this paper can be further improved in the future. Aside from hardware improvements, more investigations are advised in order to reliably reduce the error of the current relative localization filter. If this is done, it can translate into a higher freedom of movement for the MAVs without introducing higher risk in the system. Otherwise, the introduction of an additional strategy to deal with the avoidance of multiple team members should also improve performance when flying with 3 or more MAVs.

To conclude, in this work we have shown that it is possible to use wireless communication as a relative localization sensor that can be used on-board of MAVs operating in a team. This enables swarm behavior *without the need of a dedicated sensors*. Based on our results, intra-swarm collisions, a leading failure condition for MAVs flying in a limited space, can be successfully addressed by this technology provided that a collision avoidance system is used that properly encapsulates the errors involved.

## REFERENCES


[1] B. B. Mohr and D. L. Fitzpatrick, "Micro air vehicle navigation system," *Aerospace and Electronic Systems Magazine, IEEE*, vol. 23, no. 4, pp. 19–24, 2008.

[2] D. Scaramuzza, M. C. Achtelik, L. Doitsidis, F. Friedrich, E. Kosmatopoulos, A. Martinelli, M. W. Achtelik, M. Chli, S. Chatzichristofis, L. Kneip *et al.*, "Vision-controlled micro flying robots: from system design to autonomous navigation and mapping in gps-denied environments," *Robotics & Automation Magazine, IEEE*, vol. 21, no. 3, pp. 26–40, 2014.

[3] M. Achtelik, M. Achtelik, Y. Brunet, M. Chli, S. Chatzichristofis, J.-D. Decotignie, K.-M. Doth, F. Fraundorfer, L. Kneip, D. Gurdan *et al.*, "Sfly: Swarm of micro flying robots," in *Intelligent Robots and Systems (IROS), 2012 IEEE/RSJ International Conference on*. IEEE, 2012, pp. 2649–2650.

[4] V. Kumar and N. Michael, "Opportunities and challenges with autonomous micro aerial vehicles," *The International Journal of Robotics Research*, vol. 31, no. 11, pp. 1279–1291, 2012.

[5] I. Sa and P. Corke, "Vertical infrastructure inspection using a quadcopter and shared autonomy control," in *Field and Service Robotics*. Springer, 2014, pp. 219–232.

[6] B. Remes, P. Esden-Tempski, F. Van Tienen, E. Smeur, C. De Wagter, and G. De Croon, "Lisa-s 2.8 g autopilot for gps-based flight of mavs," in *IMAV 2014: International Micro Air Vehicle Conference and Competition 2014, Delft, The Netherlands, August 12-15, 2014*. Delft University of Technology, 2014.

[7] Y. Mulgaonkar, G. Cross, and V. Kumar, "Design of small, safe and robust quadrotor swarms," in *Robotics and Automation (ICRA), 2015 IEEE International Conference on*. IEEE, 2015, pp. 2208–2215.

[8] A. Kushleyev, D. Mellinger, C. Powers, and V. Kumar, "Towards a swarm of agile micro quadrotors," *Autonomous Robots*, vol. 35, no. 4, pp. 287–300, 2013.

[9] M. Brambilla, E. Ferrante, M. Birattari, and M. Dorigo, "Swarm robotics: a review from the swarm engineering perspective," *Swarm Intelligence*, vol. 7, no. 1, pp. 1–41, 2013. [Online]. Available: http://dx.doi.org/10.1007/s11721-012-0075-2

[10] V. Crespi, A. Galstyan, and K. Lerman, "Top-down vs bottom-up methodologies in multi-agent system design," *Autonomous Robots*, vol. 24, no. 3, pp. 303–313, 2008.

[11] T. Szabo, "Autonomous collision avoidance for swarms of mavs based solely on rssi measurements," Master's thesis, Delft University of Technology, 2015.

[12] A. Iyer, L. Rayas, and A. Bennett, "Formation control for cooperative localization of mav swarms," in *Proceedings of the 2013 international conference on Autonomous agents and multi-agent systems*. International Foundation for Autonomous Agents and Multiagent Systems, 2013, pp. 1371–1372.

[13] M. Varga, "Fixed-wing drones for communication networks," Ph.D. dissertation, ÉCOLE POLYTECHNIQUE FÉDÉRALE DE LAUSANNE, 2016.

[14] G. Vásárhelyi, C. Virágh, G. Somorjai, N. Tarcai, T. Szörényi, T. Nepusz, and T. Vicsek, "Outdoor flocking and formation flight with autonomous aerial robots," in *2014 IEEE/RSJ International Conference on Intelligent Robots and Systems*. IEEE, 2014, pp. 3866–3873.

[15] S. Shen, N. Michael, and V. Kumar, "Autonomous multi-floor indoor navigation with a computationally constrained mav," in *Robotics and automation (ICRA), 2011 IEEE international conference on*. IEEE, 2011, pp. 20–25.

[16] N. Michael, D. Mellinger, Q. Lindsey, and V. Kumar, "The grasp multiple micro-uav testbed," *Robotics & Automation Magazine, IEEE*, vol. 17, no. 3, pp. 56–65, 2010.

[17] A. Ledergerber, M. Hamer, and R. D'Andrea, "A robot self-localization system using one-way ultra-wideband communication," in *Intelligent Robots and Systems (IROS), 2015 IEEE/RSJ International Conference on*. IEEE, 2015, pp. 3131–3137.

[18] J. Faigl, T. Krajnik, J. Chudoba, L. Preucil, and M. Saska, "Low-cost embedded system for relative localization in robotic swarms," in *Robotics and Automation (ICRA), 2013 IEEE International Conference on*. IEEE, 2013, pp. 993–998.

[19] H. Ho, C. De Wagter, B. Remes, and G. de Croon, "Optical-flow based self-supervised learning of obstacle appearance applied to mav landing," *arXiv preprint arXiv:1509.01423*, 2015.

[20] P. Conroy, D. Bareiss, M. Beall, and J. van den Berg, "3-d reciprocal collision avoidance on physical quadrotor helicopters with on-board sensing for relative positioning," *arXiv preprint arXiv:1411.3794*, 2014.

[21] S. Roelofsen, D. Gillet, and A. Martinoli, "Reciprocal collision avoidance for quadrotors using on-board visual detection," in *Intelligent Robots and Systems (IROS), 2015 IEEE/RSJ International Conference on*. IEEE, 2015, pp. 4810–4817.

[22] T. Nageli, C. Conte, A. Domahidi, M. Morari, and O. Hilliges, "Environment-independent formation flight for micro aerial vehicles," in *Intelligent Robots and Systems (IROS 2014), 2014 IEEE/RSJ International Conference on*. IEEE, 2014, pp. 1141–1146.

[23] K. McGuire, G. de Croon, C. de Wagter, B. Remes, K. Tuyls, and H. Kappen, "Local histogram matching for efficient optical flow

computation applied to velocity estimation on pocket drones," *arXiv preprint arXiv:1603.07644*, 2016.

[24] C. De Wagter, S. Tijmons, B. D. Remes, and G. C. de Croon, "Autonomous flight of a 20-gram flapping wing mav with a 4-gram onboard stereo vision system," in *Robotics and Automation (ICRA), 2014 IEEE International Conference on*. IEEE, 2014, pp. 4982–4987.

[25] J. F. Roberts, T. Stirling, J.-C. Zufferey, and D. Floreano, "3-d relative positioning sensor for indoor flying robots," *Autonomous Robots*, vol. 33, no. 1-2, pp. 5–20, 2012.

[26] M. Basiri, "Audio-based positioning and target localization for swarms of micro aerial vehicles," 2015.

[27] M. Basiri, F. Schill, D. Floreano, and P. U. Lima, "Audio-based localization for swarms of micro air vehicles," in *Robotics and Automation (ICRA), 2014 IEEE International Conference on*. IEEE, 2014, pp. 4729–4734.

[28] M. Basiri, F. Schill, P. Lima, and D. Floreano, "On-board relative bearing estimation for teams of drones using sound," *IEEE Robotics and Automation Letters*, vol. 1, no. 2, pp. 820–827, 2016.

[29] C. Lehnert and P. Corke, "$\mu$av-design and implementation of an open source micro quadrotor," *AC on Robotics and Automation, Eds*, 2013.

[30] P. Fiorini and Z. Shiller, "Motion planning in dynamic environments using velocity obstacles," *The International Journal of Robotics Research*, vol. 17, no. 7, pp. 760–772, 1998.

[31] J. Guzzi, A. Giusti, L. M. Gambardella, G. Di Caro *et al.*, "Local reactive robot navigation: A comparison between reciprocal velocity obstacle variants and human-like behavior," in *Intelligent Robots and Systems (IROS), 2013 IEEE/RSJ International Conference on*. IEEE, 2013, pp. 2622–2629.

[32] C. Powers, D. Mellinger, A. Kushleyev, B. Kothmann, and V. Kumar, "Influence of aerodynamics and proximity effects in quadrotor flight," in *Experimental Robotics*. Springer, 2013, pp. 289–302.

[33] J. S. Seybold, *Introduction to RF propagation*. John Wiley & Sons, 2005.

[34] A. Kushki, K. Plataniotis, and A. Venetsanopoulos, "Indoor positioning with wireless local area networks (wlan)," in *Encyclopedia of GIS*. Springer, 2008, pp. 566–571.

[35] T. S. Rappaport *et al.*, *Wireless communications: principles and practice*. prentice hall PTR New Jersey, 1996, vol. 2.

[36] J. Svečko, M. Malajner, and D. Gleich, "Distance estimation using rssi and particle filter," *ISA transactions*, vol. 55, pp. 275–285, 2015.

[37] Pulse, "W1049b datasheet version 1.1," 2008, accessed November 2015. [Online]. Available: www.cdiweb.com/datasheets/pulse/W1049B.pdf

[38] K. Nguyen and Z. Luo, "Evaluation of bluetooth properties for indoor localisation," in *Progress in Location-Based Services*. Springer, 2013, pp. 127–149.

[39] C. Caron, D. Chamberland-Tremblay, C. Lapierre, P. Hadaya, S. Roche, and M. Saada, "Indoor positioning," in *Encyclopedia of GIS*. Springer, 2008, pp. 553–559.

[40] H. No, A. Cho, and C. Kee, "Attitude estimation method for small uav under accelerative environment," *GPS Solutions*, vol. 19, no. 3, pp. 343–355, 2015.

[41] M. H. Afzal, V. Renaudin, and G. Lachapelle, "Magnetic field based heading estimation for pedestrian navigation environments," in *Indoor Positioning and Indoor Navigation (IPIN), 2011 International Conference on*. IEEE, 2011, pp. 1–10.

[42] R. W. Beard, "State estimation for micro air vehicles," in *Innovations in Intelligent Machines-1*. Springer, 2007, pp. 173–199.

[43] A. M. Sabatini and V. Genovese, "A stochastic approach to noise modeling for barometric altimeters," *Sensors*, vol. 13, no. 11, pp. 15 692–15 707, 2013.

[44] K. Shilov, "The next generation design of autonomous mav flight control system smartap," in *IMAV 2014: International Micro Air Vehicle Conference and Competition 2014, Delft, The Netherlands, August 12-15, 2014*. Delft University of Technology, 2014.

[45] F. Kendoul, K. Nonami, I. Fantoni, and R. Lozano, "An adaptive vision-based autopilot for mini flying machines guidance, navigation and control," *Autonomous Robots*, vol. 27, no. 3, pp. 165–188, 2009.

[46] F. Kendoul, I. Fantoni, and K. Nonami, "Optic flow-based vision system for autonomous 3d localization and control of small aerial vehicles," *Robotics and Autonomous Systems*, vol. 57, no. 6, pp. 591–602, 2009.

[47] A. Martinelli and R. Siegwart, "Observability analysis for mobile robot localization," in *Intelligent Robots and Systems, 2005.(IROS 2005). 2005 IEEE/RSJ International Conference on*. IEEE, 2005, pp. 1471–1476.

[48] A. Martinelli, F. Pont, and R. Siegwart, "Multi-robot localization using relative observations," in *Robotics and Automation, 2005. ICRA 2005. Proceedings of the 2005 IEEE International Conference on*. IEEE, 2005, pp. 2797–2802.

[49] O. De Silva, G. K. Mann, R. G. Gosine *et al.*, "Relative localization with symmetry preserving observers," in *Electrical and Computer Engineering (CCECE), 2014 IEEE 27th Canadian Conference on*. IEEE, 2014, pp. 1–6.

[50] V. Malyavej, W. Kumkeaw, and M. Aorpimai, "Indoor robot localization by rssi/imu sensor fusion," in *Electrical Engineering/Electronics, Computer, Telecommunications and Information Technology (ECTI-CON), 2013 10th International Conference on*. IEEE, 2013, pp. 1–6.

[51] A. Cornejo and R. Nagpal, "Distributed range-based relative localization of robot swarms," in *Algorithmic Foundations of Robotics XI*. Springer, 2015, pp. 91–107.

[52] N. Point, "Inc.: Optitrack-optical motion tracking solutions," 2009.

[53] D. Wilkie, J. Van den Berg, and D. Manocha, "Generalized velocity obstacles," in *Intelligent Robots and Systems, 2009. IROS 2009. IEEE/RSJ International Conference on*. IEEE, 2009, pp. 5573–5578.

[54] D. Claes, D. Hennes, K. Tuyls, and W. Meeussen, "Collision avoidance under bounded localization uncertainty," in *Intelligent Robots and Systems (IROS), 2012 IEEE/RSJ International Conference on*. IEEE, 2012, pp. 1192–1198.

[55] J. Van den Berg, M. Lin, and D. Manocha, "Reciprocal velocity obstacles for real-time multi-agent navigation," in *Robotics and Automation, 2008. ICRA 2008. IEEE International Conference on*. IEEE, 2008, pp. 1928–1935.

[56] J. Snape, J. van den Berg, S. J. Guy, and D. Manocha, "Independent navigation of multiple mobile robots with hybrid reciprocal velocity obstacles," in *Intelligent Robots and Systems, 2009. IROS 2009. IEEE/RSJ International Conference on*. IEEE, 2009, pp. 5917–5922.

[57] ——, "The hybrid reciprocal velocity obstacle," *Robotics, IEEE Transactions on*, vol. 27, no. 4, pp. 696–706, 2011.

[58] J. Van Den Berg, S. J. Guy, M. Lin, and D. Manocha, "Reciprocal n-body collision avoidance," in *Robotics research*. Springer, 2011, pp. 3–19.

[59] G. De Croon, E. De Weerdt, C. De Wagter, B. Remes, and R. Ruijsink, "The appearance variation cue for obstacle avoidance," *Robotics, IEEE Transactions on*, vol. 28, no. 2, pp. 529–534, 2012.

[60] M. Quigley, K. Conley, B. Gerkey, J. Faust, T. Foote, J. Leibs, R. Wheeler, and A. Y. Ng, "Ros: an open-source robot operating system," in *ICRA workshop on open source software*, vol. 3, no. 3.2, 2009, p. 5.

[61] N. Koenig and A. Howard, "Design and use paradigms for gazebo, an open-source multi-robot simulator," in *Intelligent Robots and Systems, 2004.(IROS 2004). Proceedings. 2004 IEEE/RSJ International Conference on*, vol. 3. IEEE, 2004, pp. 2149–2154.

[62] J. Meyer, A. Sendobry, S. Kohlbrecher, U. Klingauf, and O. Von Stryk, "Comprehensive simulation of quadrotor uavs using ros and gazebo," in *Simulation, Modeling, and Programming for Autonomous Robots*. Springer, 2012, pp. 400–411.

[63] M. Mueller and A. Drouin, "Paparazzithe free autopilot. build your own uav," in *24th Chaos Communication Congress, Berliner Congress Center, Dec*, 2007, pp. 27–30.

[64] P. Brisset and G. Hattenberger, "Multi-uav control with the paparazzi system," in *HUMOUS 2008, Conference on Humans Operating Unmanned Systems*, 2008.

[65] Parrot, "Ar drone 2.0," 2012. [Online]. Available: http://ardrone2.parrot.com

[66] BlueGiga, "Bled112 bluetooth smart dongle," 2016. [Online]. Available: https://www.bluegiga.com/en-US/products/bled112-bluetooth-smart-dongle

[67] T. Gaugel, J. Mittag, H. Hartenstein, S. Papanastasiou, and E. G. Strom, "In-depth analysis and evaluation of self-organizing tdma," in *Vehicular Networking Conference (VNC), 2013 IEEE*. IEEE, 2013, pp. 79–86.

[68] K. Townsend, C. Cufí, R. Davidson *et al.*, *Getting started with Bluetooth low energy: Tools and techniques for low-power networking*. O'Reilly Media, Inc., 2014.

[69] A. Kallapur, I. Petersen, and S. Anavatti, "A discrete-time robust extended kalman filter," in *American Control Conference, 2009. ACC'09.* IEEE, 2009, pp. 3819–3823.

[70] J. Sasiadek and Q. Wang, "Sensor fusion based on fuzzy kalman filtering for autonomous robot vehicle," in *Robotics and Automation, 1999. Proceedings. 1999 IEEE International Conference on*, vol. 4. IEEE, 1999, pp. 2970–2975.

[71] E. A. Wan and R. Van Der Merwe, "The unscented kalman filter for nonlinear estimation," in *Adaptive Systems for Signal Processing, Communications, and Control Symposium 2000. AS-SPCC. The IEEE 2000*. Ieee, 2000, pp. 153–158.

[72] S. J. Julier, "The scaled unscented transformation," in *American Control Conference, 2002. Proceedings of the 2002*, vol. 6. IEEE, 2002, pp. 4555–4559.

[73] A. Assa and F. Janabi-Sharifi, "A kalman filter-based framework for enhanced sensor fusion," *Sensors Journal, IEEE*, vol. 15, no. 6, pp. 3281–3292, 2015.

[74] L. DAlfonso, W. Lucia, P. Muraca, and P. Pugliese, "Mobile robot localization via ekf and ukf: A comparison based on real data," *Robotics and Autonomous Systems*, vol. 74, pp. 122–127, 2015.

[75] F. M. Dekking, *A Modern Introduction to Probability and Statistics: Understanding why and how*. Springer Science & Business Media, 2005.